

Monotone Curve Estimation via Convex Duality

Tongseok Lim*

Mitch Daniels School of Business, Purdue University, USA

Kyeongsik Nam

Department of Mathematical Sciences, KAIST, South Korea

and

Jinwon Sohn

Department of Statistics, Purdue University, USA

January 12, 2025

Abstract

A principal curve serves as a powerful tool for uncovering underlying structures of data through 1-dimensional smooth and continuous representations. On the basis of optimal transport theories, this paper introduces a novel principal curve framework constrained by monotonicity with rigorous theoretical justifications. We establish statistical guarantees for our monotone curve estimate, including expected empirical and generalized mean squared errors, while proving the existence of such estimates. These statistical foundations justify adopting the popular early stopping procedure in machine learning to implement our numeric algorithm with neural networks. Comprehensive simulation studies reveal that the proposed monotone curve estimate outperforms competing methods in terms of accuracy when the data exhibits a monotonic structure. Moreover, through two real-world applications on future prices of copper, gold, and silver, and avocado prices and sales volume, we underline the robustness of our curve estimate against variable transformation, further confirming its effective applicability for noisy and complex data sets. We believe that this monotone curve-fitting framework offers significant potential for numerous applications where monotonic relationships are intrinsic or need to be imposed.

Keywords: Principal Curve, Statistical Error Analysis, Optimal Transport, Neural Network

*The authors gratefully acknowledge the support of the National Research Foundation of Korea (RS-2019-NR040050).

1 Introduction

A principal curve is a 1-dimensional manifold penetrating the middle of data. In mathematics, a general curve is defined as a vector of functions where an index parameter draws the shape of each component function. For example, we can parametrize a unit circle as $(\cos s, \sin s)$, or a quadratic curve in \mathbb{R}^2 as a vector of (s, s^2) , where $s \in \mathbb{R}$ denotes the index parameter. Similarly, a principal curve is a 1-dimensional manifold of multivariate random variables whose probability law relies on the index parameter. A representative example is a multivariate Gaussian distribution whose mean vector varies by the index parameter. In this regard, a principal curve captures the essential geometric shape of data, and it also provides curve-sense summary statistics to analyze joint relationships between variables rather than conditional relationships. The latter characteristic of a principal curve can be particularly beneficial when causal relationships between variables are ambiguous, which occurs a lot in numerous real-world problems.

Various fields harness such characteristics of a principal curve in data analysis. Banfield and Raftery (1992) clustered principal curves to outline distinctive floes in a satellite image as an image processing method. In the field of transportation, Einbeck and Dwyer (2011) analyzed the relationship between vehicles' speed and traffic flow by curves since the two key variables are hardly seen to have a causal relationship with each other but rather a latent variable traffic density associates the target variables. Also, for pathway-level analysis on cancer progression, Drier et al. (2013) projected normal and tumor samples on a principal curve estimated from the principal components of the two contrasting samples and showed the distance along the curve between the samples reveals important findings on cancer data analysis. Chen et al. (2015) employed a principal curve technique to detect and compare cosmic filaments from densities of the galaxy and dark matter. For more

examples of using principal curves for data analysis, we refer to Takei et al. (2021); Layton et al. (2022); Ghazanfar et al. (2024).

While the literature on principal curves becomes more mature, the concept of a principal curve constrained to exhibit a monotonic shape remains underexplored. Monotonic relationships between variables are prevalent in numerous real-world scenarios, addressing the practical importance of estimating a monotone principal curve for reliable analysis. For instance, demand and supply curves in economics illustrate inverse and direct relationships between price and quantity. Arfaoui and Ben Rejeb (2017) analyzed the interdependencies between oil, gold, US dollars, and the stock market through a simultaneous equation model, which justifies that each variable relates positively or negatively to other variables. As addressed in Patton and Timmermann (2010), a plethora of theories in financial modeling require monotonic situations such as discovering the relation between expected returns and market betas in the capital asset pricing model. In ethics-considered machine learning, such as for privacy or fairness, ethical improvement of a learned model tends to trade off its utility such as degree of accuracy in general (Xie et al., 2018; Sohn et al., 2024). These real-world problems highlight the potential utility of monotone principal curves as fundamental data analysis tools when monotonic phenomena between variables are expected.

Our contributions are mainly threefold. First, we propose a novel principal curve framework for fitting a monotonic curve in Section 2. To begin with, we characterize the monotone curve in arbitrary finite-dimensional space using convex analysis and monotone operator theory, and then we propose an optimization problem to find the monotone curve. Secondly, Section 3 places rigorous theoretical analysis on the curve estimate, the solution of the established optimization. After verifying the existence of the solution, we disclose the convergence rate of the expected empirical and generalization errors. The generalization

error in this work implies the estimation error for unseen data. Note that tackling such a generalization error is particularly important from machine learning and statistics viewpoints, since it can provide a theoretical foundation for model selection to avoid overfitting or find optimal hyperparameters. To our knowledge, this is the first work in the principal curve literature to derive the generalization error based on convex analysis. Finally, in Section 4, we introduce a numerical algorithm that finds the monotone curve through neural networks. In Section 5, simulation studies verify that our method achieves more accurate estimation than general curve-fitting methods when the underlying curve is monotone. Section 6 applies the proposed framework to model future prices for copper, gold, and silver, and to estimate a demand curve between avocado prices and sales volume. These real data applications advertise that our method enjoys more robust estimation in terms of variable transformation than the competing methods when monotone relationships are anticipated.

1.1 Literature review

To seek a better representation of a principal curve, versatile approaches have been steadily attempted and categorized mainly by two branches from our perspective. First, a principal curve is seen as a minimizer of a distance between the curve and data points with regularization. Secondly, a principal curve is approached by a ridge where gradients and eigenvectors of a density’s Hessian are orthogonal. The seminal work of Hastie and Stuetzle (1989) defined a curve on self-consistency as a local average of data points having the minimal mean squared distance to the data points indexed by the domain of the curve itself. This initial approach, however, guarantees the existence of a curve only on a specific data distribution and tends to estimate a biased curve around high-curvature areas. These limitations ignited subsequent studies. To alleviate the bias, Tibshirani (1992) approached a principal

curve as weighted local averages of data points by formulating the curve-generating process as a probabilistic mixture modeling. Banfield and Raftery (1992) eased the bias by updating a curve estimate based on the smoothed residuals of the curve. To ensure the existence of a curve in a more general distribution, Kégl et al. (2000) considered a curve whose length is bounded by a fixed size on a bounded and convex domain. Gerber and Whitaker (2013) proposed a surrogate objective to replace the mean squared distance so that a principal curve lies in critical points that are locally minimal. In behind, Duchamp and Stuetzle (1996) showed the self-consistent curve can be critical but not extremal points for the mean squared distance, which contributed to justifying such challenges of estimating self-consistent curves. Recent efforts in this branch have focused on finding self-consistent curves in non-Euclidean spaces (Hauberg, 2015; Lee et al., 2020; Kang and Oh, 2024).

On the one hand, Ozertem and Erdogmus (2011) viewed a principal curve, for a given probability density function, to lie in an 1-dimensional intrinsic space in which the density’s gradient and eigenvectors of the Hessian are constrained to be orthogonal. The set of points in the constrained space is called a ridge or filament that captures the essential structures of the data (Hall et al., 1992; Eberly et al., 1994; Qiao and Polonik, 2016). In general, ridges refer to multidimensional constrained spaces where the projected gradient of the density vanishes in certain directions defined by the Hessian eigenvectors, and the curvature satisfies specific eigenvalue constraints. Note the filament stands for the 1-dimensional ridge. Genovese et al. (2014) mathematically justified that this subspace-constrained approach that finds a ridge can approximate the true lower-dimensional manifold with an additive noise term. Chen et al. (2015) suggested selecting a reasonable kernel’s bandwidth used to approximate the probability density by maximizing the extent of covering a population ridge. On the other hand, Qiao and Polonik (2016) viewed the 1-dimensional ridge as an

integral curve from the differential equation involving the Hessian’s eigenvector corresponding to the second eigenvalue in the two-dimensional space. Besides, further efforts have been made to improve the algorithmic computation and theory of the subspace-constrained methodology (Qiao and Polonik, 2021; Zhang and Chen, 2023).

2 Formulation of monotone curve-fitting task

The construction of our monotone curve-fitting task starts with characterizing a monotone curve in a finite-dimensional space through convex analysis. Then a novel learning problem is introduced where the solution corresponds to the suggested monotone curve.

2.1 Monotone set and diagonal parametrization

Let $[n] := \{1, 2, \dots, n\}$ for $n \in \mathbb{N} = \{1, 2, \dots\}$. Let $\mathcal{P}(\Omega)$ denote the set of probability measures (distributions) over a measure space Ω , and $\langle \mathbf{a}, \mathbf{b} \rangle$ denote the inner product of vectors \mathbf{a}, \mathbf{b} . We say that a set $\Gamma \subset \mathbb{R}^k$ is *monotone* if for any $\mathbf{a} = (a_i)_i, \mathbf{b} = (b_i)_i \in \mathbb{R}^k$, either $a_i \geq b_i$ or $a_i \leq b_i$ for all $i \in [k]$. Note that this is equivalent to $(b_j - a_j)(b_i - a_i) \geq 0$ for all $i, j \in [k]$. A monotone set Γ is *maximally monotone* if it is not a proper subset of other monotone sets.

Now we characterize a monotone curve via the diagonal coordinate $s(\mathbf{x}) := \sum_{i=1}^k x_i, \forall \mathbf{x} = (x_1, \dots, x_k) \in \mathbb{R}^k$. Let $S(\Gamma) := \{s(\mathbf{x}) \mid \mathbf{x} \in \Gamma\}$ and $s_\Gamma : \Gamma \rightarrow S(\Gamma)$, the restriction of s on Γ .

Definition 2.1 *For a monotone set $\Gamma \subseteq \mathbb{R}^k$, we call $\gamma = (\gamma_1, \dots, \gamma_k) := s_\Gamma^{-1} : S(\Gamma) \rightarrow \Gamma$ the associated monotone curve, which parametrizes Γ via the diagonal coordinate s .*

Note that s_Γ is bijective and each component γ_i is a nondecreasing function of s if Γ is monotone, and the maximal monotonicity of Γ is equivalent to the condition $S(\Gamma) = \mathbb{R}$. Our definition of a monotone curve is based on an underlying monotone set. In the following,

we outline the characterization of a monotone set using convex functions that satisfy a duality relationship, and show that the associated curve γ can be represented by them.

2.2 Exposure of a monotone set through convex functions

We first introduce basic mathematical tools for convex analysis. Let $\mathcal{A}(\mathcal{H})$ denote the set of proper, lower-semicontinuous and convex functions (valued in $\mathbb{R} \cup \{+\infty\}$) on a Hilbert space \mathcal{H} . In this general setting, a set $\Gamma \subset \mathcal{H} \times \mathcal{H}$ is called monotone if $\langle b_2 - a_2, b_1 - a_1 \rangle \geq 0$ for any $\mathbf{a} = (a_1, a_2), \mathbf{b} = (b_1, b_2) \in \Gamma$. For a function $f : \mathcal{H} \rightarrow \mathbb{R} \cup \{+\infty\}$, its convex conjugate is $f^*(\mathbf{y}) := \sup_{\mathbf{x} \in \mathcal{H}} [\langle \mathbf{x}, \mathbf{y} \rangle - f(\mathbf{x})]$. Then the Fenchel-Young inequality $f(\mathbf{x}) + f^*(\mathbf{y}) \geq \langle \mathbf{x}, \mathbf{y} \rangle$ holds for all $\mathbf{x}, \mathbf{y} \in \mathcal{H}$. We say that f and g are *mutually conjugate* if $f = g^*$ and $g = f^*$. The Fenchel–Moreau theorem states that $f^{**} := (f^*)^* = f$ for any $f \in \mathcal{A}(\mathcal{H})$, which implies f and f^* are mutually conjugate. For $f \in \mathcal{A}(\mathcal{H})$ and $\mathbf{x} \in \mathcal{H}$, the *subdifferential* of f at \mathbf{x} is defined as the following convex set $\partial f(\mathbf{x}) = \{\mathbf{v} \in \mathcal{H} \mid f(\mathbf{y}) - f(\mathbf{x}) \geq \langle \mathbf{v}, \mathbf{y} - \mathbf{x} \rangle \forall \mathbf{y} \in \mathcal{H}\}$, and the set $\partial f = \bigcup_{\mathbf{x} \in \mathcal{H}} \{(\mathbf{x}, \mathbf{y}) \in \mathcal{H} \times \mathcal{H} \mid \mathbf{y} \in \partial f(\mathbf{x})\}$ is then called the subdifferential of f .

The following proposition by Rockafellar and Minty (see Bauschke and Combettes (2019)) states that a monotone set is contained in a set where the Fenchel-Young inequality achieves equality. Let $S(\Gamma) = \{\mathbf{x} + \mathbf{y} \mid (\mathbf{x}, \mathbf{y}) \in \Gamma\}$ and $\Gamma^{-1} := \{(\mathbf{y}, \mathbf{x}) \mid (\mathbf{x}, \mathbf{y}) \in \Gamma\}$ for $\Gamma \subset \mathcal{H}^2$.

Proposition 2.1 *Let $f, g \in \mathcal{A}(\mathcal{H})$ satisfy $f(x) + g(y) \geq \langle x, y \rangle$ for all $x, y \in \mathcal{H}$. Then the contact set $\Gamma_{f,g} := \{(x, y) \in \mathcal{H}^2 \mid f(x) + g(y) = \langle x, y \rangle\}$ is monotone. Moreover, f, g are mutually conjugate if and only if $\Gamma_{f,g}$ is maximally monotone if and only if $S(\Gamma_{f,g}) = \mathcal{H}$, in which case $\Gamma_{f,f^*} = \partial f = (\partial f^*)^{-1}$. Furthermore, any monotone set $\Gamma \subset \mathcal{H}^2$ is contained in a maximally monotone set Γ_{f,f^*} for some $f \in \mathcal{A}(\mathcal{H})$.*

The equality $\partial f = (\partial f^*)^{-1}$ states that for $f \in \mathcal{A}(\mathcal{H})$, ∂f and ∂f^* are the (generalized) inverses of each other.

Understanding how to obtain such f and f^* that expose a given monotone set Γ as $\Gamma \subset \Gamma_{f,f^*}$ is particularly simple and instructive when $\mathcal{H} = \mathbb{R}$. To simplify discussion, we suppose that $\Gamma \subset \mathbb{R}^2$ is monotone and Γ is maximally monotone without loss of generality.

Remark 2.1 (Construction of f, f^* given Γ) *Given a maximally monotone $\Gamma \subset \mathbb{R}^2$, we define convex functions f, g such that $H_{f,g}(x, y) := f(x) + g(y) - xy \geq 0$ for all $x, y \in \mathbb{R}$, and moreover, $\Gamma = \{(x, y) \in \mathbb{R}^2 \mid H_{f,g}(x, y) = 0\}$. As a result, f, g are mutually conjugate due to the maximality of Γ . For simplicity, we assume Γ is strictly monotone, i.e., $(x' - x)(y' - y) > 0$ for any $(x, y), (x', y') \in \Gamma$. We also assume that $\{x \mid (x, y) \in \Gamma\} = \{y \mid (x, y) \in \Gamma\} = \mathbb{R}$. Then Γ is the graph of a continuous, strictly increasing function (still denoted as Γ), i.e., $\Gamma = \{(x, y) \mid y = \Gamma(x), x \in \mathbb{R}\}$. Also, Γ has a unique intersection point with y -axis; denote it as $(0, y_0)$. Now define $f(x) := \int_0^x \Gamma(u) du$ and $g(y) := \int_{y_0}^y \Gamma^{-1}(u) du$. Then f, g are convex as Γ is increasing, and $\partial g = (\partial f)^{-1}$ implies that f, g are mutually conjugate, i.e., $g = f^*$.*

2.3 Loss function to extract a monotone set

Such procedures for characterizing a monotone set through mutually conjugate convex functions lay the groundwork for designing a novel statistical learning framework to identify a monotone principal curve. It is helpful to first discuss this problem in the two-dimensional space \mathbb{R}^2 . Let $\mu \in \mathcal{P}(\mathbb{R}^2)$ denote the data distribution of $\mathbf{X} = (X_1, X_2)$, which exhibits an approximately monotone structure. To formulate a learning framework, this work proposes the following “loss function” to identify a monotone set:

$$H(\mathbf{x}; f_1, f_2) = f_1(x_1) + f_2(x_2) - x_1 x_2, \quad \mathbf{x} = (x_1, x_2) \in \mathbb{R}^2$$

where f_1 and f_2 are in duality defined as below.

Definition 2.2 *We say that a pair of convex functions $f_1, f_2 \in \mathcal{A}(\mathbb{R})$ is in duality position, or simply in duality, if $H(\mathbf{x}; f_1, f_2) \geq 0$, i.e., $f_1(x_1) + f_2(x_2) \geq x_1 x_2$ for all $x_1, x_2 \in \mathbb{R}$.*

This loss function will be generally larger as \mathbf{x} is farther from the monotone set Γ_{f_1, f_2} on which H attains its minimum 0. Figure 1 draws a contour of $H(\mathbf{x}; f, f^*)$ for a power function on the grid of x_1, x_2 . This inspires us to use $\mathbb{E}_{\mathbf{x} \sim \mu}[H(\mathbf{X}; f_1, f_2)]$ as an objective

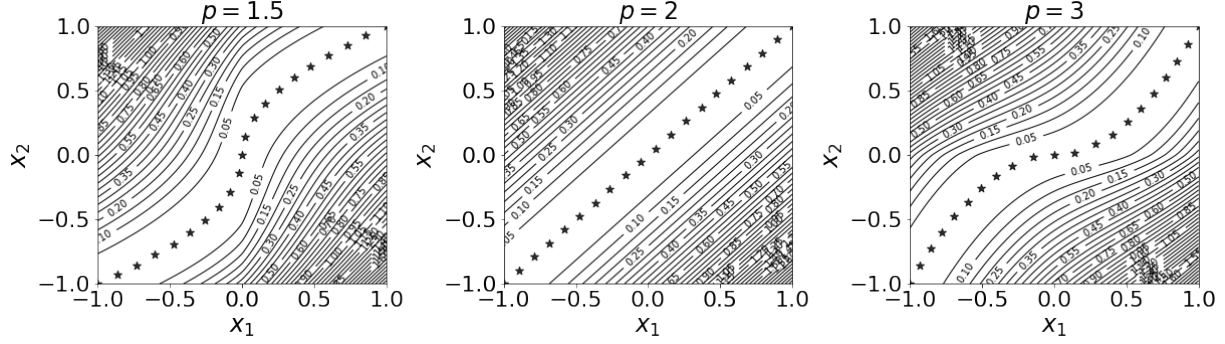


Figure 1: Contour of $H(\mathbf{x}; f, f^*)$: $f(x) = |x|^p/p$ and $f^*(x) = |x|^q/q$, the convex conjugate of f , with $1/p + 1/q = 1$. The star points (★) represent the zero set where $H(\mathbf{x}; f, f^*) = 0$.

and minimize it over the convex pair f_1, f_2 in duality, since Proposition 2.1 shows that the zero set Γ_{f_1, f_2} will then represent a monotone curve in \mathbb{R}^2 . Later, we will present a generalized formulation for higher dimensions \mathbb{R}^k in (2) and (3).

We now explain how the diagonal parametrization (monotone curve) $\gamma = s_\Gamma^{-1} : S(\Gamma) \rightarrow \Gamma$ can be represented by a convex pair (f_1, f_2) . If (f_1, f_2) is in duality and $\mathbf{x} = (x_1, x_2)$, the first order condition yields the following implication

$$H(\mathbf{x}; f_1, f_2) = 0 \implies x_2 \in \partial f_1(x_1) \text{ and } x_1 \in \partial f_2(x_2). \quad (1)$$

With $q(x) := |x|^2/2$ and $g_i := f_i + q$, $i = 1, 2$, the following equivalences $x_2 \in \partial f_1(x_1) \iff x_1 + x_2 \in \partial g_1(x_1)$ and $x_1 \in \partial f_2(x_2) \iff x_1 + x_2 \in \partial g_2(x_2)$ are straightforward. Hence, the implication (1) can be restated as $\mathbf{x} \in \Gamma_{f_1, f_2} \implies x_i = (\partial g_i)^{-1}(s(\mathbf{x}))$, $i = 1, 2$. In fact, the reverse implication also holds; see (Bartz et al., 2021, Theorem 4.1) and its proof.

This shows that the diagonal parametrization $\gamma = (\gamma_1, \gamma_2)$ of the monotone set Γ_{f_1, f_2} can be expressed as $\gamma_i = (\partial g_i)^{-1}$. Moreover, $(\partial g_i)^{-1} = \nabla g_i^*$, where (whether $g_i \in \mathcal{A}(\mathbb{R})$ is differen-

tiable or not) $g_i^* = f_i^* \square q := \inf_{y \in \mathbb{R}} [f_i^*(y) + q(x-y)]$, called the Moreau envelope of f_i^* , is a differentiable convex function on \mathbb{R} with 1-Lipschitz nondecreasing derivative ∇g_i^* (Bauschke and Combettes (2019)). Hence the monotone curve $\gamma(s) := ((\partial g_1)^{-1}(s), (\partial g_2)^{-1}(s))$ is defined for all $s \in \mathbb{R}$, with $((\partial g_1)^{-1}(s), (\partial g_2)^{-1}(s)) \in \Gamma_{f_1, f_2}$ if $s \in S(\Gamma_{f_1, f_2})$. In particular, if $f_1 = f = f_2^*$, then since $S(\Gamma_{f, f^*}) = \mathbb{R}$, γ yields a bijection between \mathbb{R} and Γ_{f, f^*} .

2.4 Exposure of a monotone curve in higher dimensions

This section extends the aforementioned discussion to any data dimension k . For $f_i \in \mathcal{A}(\mathbb{R})$, $i \in [k]$, we write $\mathbf{f} = (f_1, \dots, f_k)$ and $f^\oplus(\mathbf{x}) := \sum_{i=1}^k f_i(x_i)$ for $\mathbf{x} = (x_1, \dots, x_k) \in \mathbb{R}^k$. Define a cost function $c(\mathbf{x}) := \sum_{1 \leq i < j \leq k} x_i x_j$ and $H(\mathbf{x}; \mathbf{f}) := f^\oplus(\mathbf{x}) - c(\mathbf{x}) = \sum_{i=1}^k f_i(x_i) - \sum_{1 \leq i < j \leq k} x_i x_j$. Let us say that \mathbf{f} is in *duality position*, or simply *in duality*, if the nonnegativity $H(\mathbf{x}; \mathbf{f}) \geq 0$ holds for all $\mathbf{x} \in \mathbb{R}^k$. Also we say that $\mathbf{f} = (f_1, \dots, f_k)$ is a *c-conjugate tuple* if for each $i \in [k]$ and $x_i \in \mathbb{R}$, $f_i(x_i) = (\oplus_{j \neq i} f_j)^c(x_i) := \sup_{x_j \in \mathbb{R}} [c(x_1, \dots, x_i, \dots, x_k) - \sum_{j \neq i} f_j(x_j)]$. Any *c-conjugate tuple* is in duality position. Also, $(\oplus_{j \neq i} f_j)^c$ is convex and lower-semicontinuous for any proper (not necessarily convex) functions $(f_j)_j$, thus $(\oplus_{j \neq i} f_j)^c \in \mathcal{A}(\mathbb{R})$ if proper.

Remark 2.2 Let $q(x) = x^2/2$, $g_i = f_i + q$. We then have $H(\mathbf{x}; \mathbf{f}) = \tilde{H}(\mathbf{x}; \mathbf{g})$ with $\tilde{H}(\mathbf{x}; \mathbf{g}) := g^\oplus(\mathbf{x}) - \tilde{c}(\mathbf{x})$ and $\tilde{c}(\mathbf{x}) := s(\mathbf{x})^2/2$. As a result, \mathbf{f} is *c-conjugate* if and only if \mathbf{g} is \tilde{c} -conjugate.

The following is an extension of Proposition 2.1 for the *c-conjugate* functions on \mathbb{R} .

Proposition 2.2 Assume that $\mathbf{f} = (f_i)_{i=1}^k \in \mathcal{A}(\mathbb{R})^k$ is in duality position. Then the zero set $\Gamma_{\mathbf{f}} := \{\mathbf{x} \in \mathbb{R}^k \mid H(\mathbf{x}; \mathbf{f}) = 0\}$ is monotone. Moreover, \mathbf{f} is a *c-conjugate tuple* if and only if $\Gamma_{\mathbf{f}}$ is maximally monotone if and only if $S(\Gamma_{\mathbf{f}}) = \mathbb{R}$. Furthermore, any monotone set $\Gamma \subset \mathbb{R}^k$ is contained in a maximally monotone set $\Gamma_{\mathbf{f}}$ for some *c-conjugate tuple* $\mathbf{f} \in \mathcal{A}(\mathbb{R})^k$.

The monotonicity of $\Gamma_{\mathbf{f}}$ is shown in Lemma ?? in Supplementary ??. The proposition shows that any monotone curve in \mathbb{R}^k can be exposed as a subset of the monotone set $\Gamma_{\mathbf{f}}$

induced by convex functions \mathbf{f} in duality, and $\Gamma_{\mathbf{f}}$ is maximally monotone if and only if \mathbf{f} is c -conjugate. This motivates us to use $H(\mathbf{x}; \mathbf{f})$ as the objective function. We note that Remark 2.1 can also be extended for \mathbb{R}^k . This is outlined in Supplementary ??.

To characterize a monotone curve γ in \mathbb{R}^k , we turn to the parametrization of monotone sets in \mathbb{R}^k using the diagonal coordinate. Given $f_i \in \mathcal{A}(\mathbb{R})$, $i \in [k]$, with $H(\cdot; \mathbf{f}) \geq 0$ and $\mathbf{x} = (x_1, \dots, x_k) \in \mathbb{R}^k$, the equivalence $H(\mathbf{x}; \mathbf{f}) = 0 \iff s(\mathbf{x}) \in \partial g_i(x_i) \forall i \in [k]$ holds true by an application of Theorem 4.1 of Bartz et al. (2021). This yields a parametrization of the monotone set $\Gamma_{\mathbf{f}}$ via the diagonal coordinate, i.e., $\mathbf{x} \in \Gamma_{\mathbf{f}} \iff x_i = (\partial g_i)^{-1}(s(\mathbf{x}))$, $\forall i \in [k]$, where $(\partial g_i)^{-1} = \nabla g_i^* = \nabla(f_i^* \square q)$ is a 1-Lipschitz nondecreasing function on \mathbb{R} . We can thus write $\gamma(s) = \gamma_{\mathbf{f}}(s) := ((\partial g_i)^{-1}(s))_{i \in [k]}$. If \mathbf{f} is c -conjugate, then $\gamma: \mathbb{R} \rightarrow \Gamma_{\mathbf{f}}$ is a bijection.

2.5 Monotone curve-fitting task

The diagonal parametrization motivates another natural form for the objective function $\|\mathbf{x} - \gamma_{\mathbf{f}}(s(\mathbf{x}))\|^2$. Intuitively, $\gamma_{\mathbf{f}}$ minimizing the squared error can be seen as a 1-dimensional latent manifold that condenses the original information of the data points. This extra term, therefore, helps $\gamma_{\mathbf{f}}$ represent the essential geometric shape of the data points. In manifold learning, this term is commonly referred to as a reconstruction error, representing the extent to which a model can accurately reproduce the original data. Consequently, we propose the following optimization problem for the monotone curve-fitting task (for a chosen parameter $\lambda \geq 0$ and a domain $\mathcal{D} \subset \mathcal{A}(\mathbb{R})$):

$$\text{minimize } \mathbb{E}_{\mathbf{X} \sim \mu} [H(\mathbf{X}; \mathbf{f}) + \lambda \|\mathbf{X} - \gamma_{\mathbf{f}}(s(\mathbf{X}))\|^2] \text{ over } \mathbf{f} = (f_1, \dots, f_k) \in \mathcal{D}^k \text{ in duality.} \quad (2)$$

As before, if we restrict \mathbf{f} to be c -conjugated, then the problem is expressed as

$$\text{minimize } \mathbb{E}_{\mathbf{X} \sim \mu} [H(\mathbf{X}; \mathbf{f}) + \lambda \|\mathbf{X} - \gamma_{\mathbf{f}}(s(\mathbf{X}))\|^2] \text{ over } c\text{-conjugate tuples } \mathbf{f} \in \mathcal{D}^k. \quad (3)$$

As a result, the solution curve $\gamma_{\mathbf{f}}$ becomes restricted to be monotone in $\Gamma_{\mathbf{f}}$ while having a minimal distance to the data.

This penalty-based optimization categorizes our monotone curve-fitting task to the first branch in the curve literature discussed in Section 1.1. More specifically, the self-consistency curve γ_{SC} of Hastie and Stuetzle (1989) can also be seen to minimize the reconstruction error $\mathbb{E}[\|\mathbf{X} - \gamma_{\text{SC}}(s)\|^2]$ in the sense that their approach is to find the projection index that has smaller reconstruction error $s_{\gamma_{\text{SC}}}(\mathbf{X}) := \sup\{s : \|\mathbf{X} - \gamma_{\text{SC}}(s)\| = \inf_{s'} \|\mathbf{X} - \gamma_{\text{SC}}(s')\|\}$ where $\gamma_{\text{SC}}(s) = \mathbb{E}[\mathbf{X} | s_{\gamma_{\text{SC}}}(\mathbf{X}) = s]$. In our case, we specify the diagonal coordinate, which is not a variable of optimization, but still maintains the data-driven nature by summing all variables. Similarly, other methodologies in this branch formulate constrained optimization to define and find principal curves (Tibshirani, 1992; Kégl et al., 2000; Hauberg, 2015).

In conclusion, we propose the following monotone curve-fitting task.

Task 1 *Given data $\widehat{\mu} \in \mathcal{P}(\mathbb{R}^k)$, solve (2) or (3) to find a minimizer of convex functions $\widehat{\mathbf{f}} = (\widehat{f}_1, \dots, \widehat{f}_k)$. The parametrized monotone curve $\widehat{\gamma}(s) := ((\partial \widehat{g}_i)^{-1}(s))_{i \in [k]}$ is offered as a solution for the monotone curve-fitting task, where $\widehat{g}_i = \widehat{f}_i + q$.*

2.5.1 Extension of Task 1 via orthogonal transformation

What can we do if, for instance, the observed data in \mathbb{R}^2 does not exhibit rough monotonicity but instead aligns with an anti-monotone structure, such as along the anti-diagonal? In cases where the data appears to be roughly aligned along an axis that is not parallel to the diagonal, one could consider applying Task 1 after performing an appropriate *rotation of the data*. We denote by $\mathcal{O}(k) = \{U \in \mathbb{R}^{k \times k} \mid U^\top U = U U^\top = I\}$ the set of all orthogonal matrices, where U^\top is the transpose of U and I is the identity matrix. Then for $\mathbf{f} = (f_1, \dots, f_k) \in \mathcal{D}^k$ with a chosen domain $\mathcal{D} \subset \mathcal{A}(\mathbb{R})$, the problems (2) and (3) can be generalized as

$$\text{minimize } \mathbb{E}_{\mathbf{X} \sim \mu} [H(U\mathbf{X}; \mathbf{f}) + \lambda \|U\mathbf{X} - \gamma_{\mathbf{f}}(s(U\mathbf{X}))\|^2] \text{ over } U \in \mathcal{O}(k) \text{ and } \mathbf{f} \text{ in duality,} \quad (4)$$

$$\text{minimize } \mathbb{E}_{\mathbf{X} \sim \mu} [H(U\mathbf{X}; \mathbf{f}) + \lambda \|U\mathbf{X} - \gamma_{\mathbf{f}}(s(U\mathbf{X}))\|^2] \text{ over } U \in \mathcal{O}(k) \text{ and } c\text{-conjugate } \mathbf{f}, \quad (5)$$

respectively. Consequently, we propose the following modified task.

Task 2 *Given data $\hat{\mu} \in \mathcal{P}(\mathbb{R}^k)$, solve (4) or (5) to find a minimizer of an orthogonal transformation \hat{U} and convex functions $\hat{\mathbf{f}} = (\hat{f}_1, \dots, \hat{f}_k)$. The parametrized monotone curve $s \mapsto \hat{U}^\top \hat{\gamma}(s)$, where $\hat{\gamma}(s) = ((\partial \hat{g}_i)^{-1}(s))_{i \in [k]}$ and $\hat{g}_i = \hat{f}_i + q$, is offered as a solution.*

To motivate this task, we illustrate Task 2 on a toy example in Figure 2. A toy data set follows a bivariate normal variable $\mathbf{X}(s) = (X_1(s), X_2(s))^\top$ where $\mathbb{E}[X_1(s)] = -s^2$, $\mathbb{E}[X_2(s)] = \log(s+1)$, $\text{Var}(X_1(s)) = \text{Var}(X_2(s)) = 0.1$, and $\text{Cov}(X_1(s), X_2(s)) = 0.09$ for $s \sim \text{Unif}[0, 3]$. Note that the ground truth curve of \mathbf{X} is expressed by $(-s^2, \log(s+1))^\top$. The original data points are positioned antidiagonally (left-top figure), which causes the transformation U to align the transformed data points diagonally. On top of that, the contour of H exposes the monotone set. Once the task finds the monotone curve, the estimated curve in the space of $U\mathbf{X}$ is rotated back to estimate the curve in the space of \mathbf{X} . Depending on a goal of an application, this final step may not be necessary if one wants to find a monotone curve on the space of $U\mathbf{X}$ or find U to make variables monotonically related. A numeric algorithm to implement Task 2 appears in Section 4 later, where we use the first principal components of \mathbf{X} to determine the initial value of U and optimize it with other variables for sufficient flexibility.

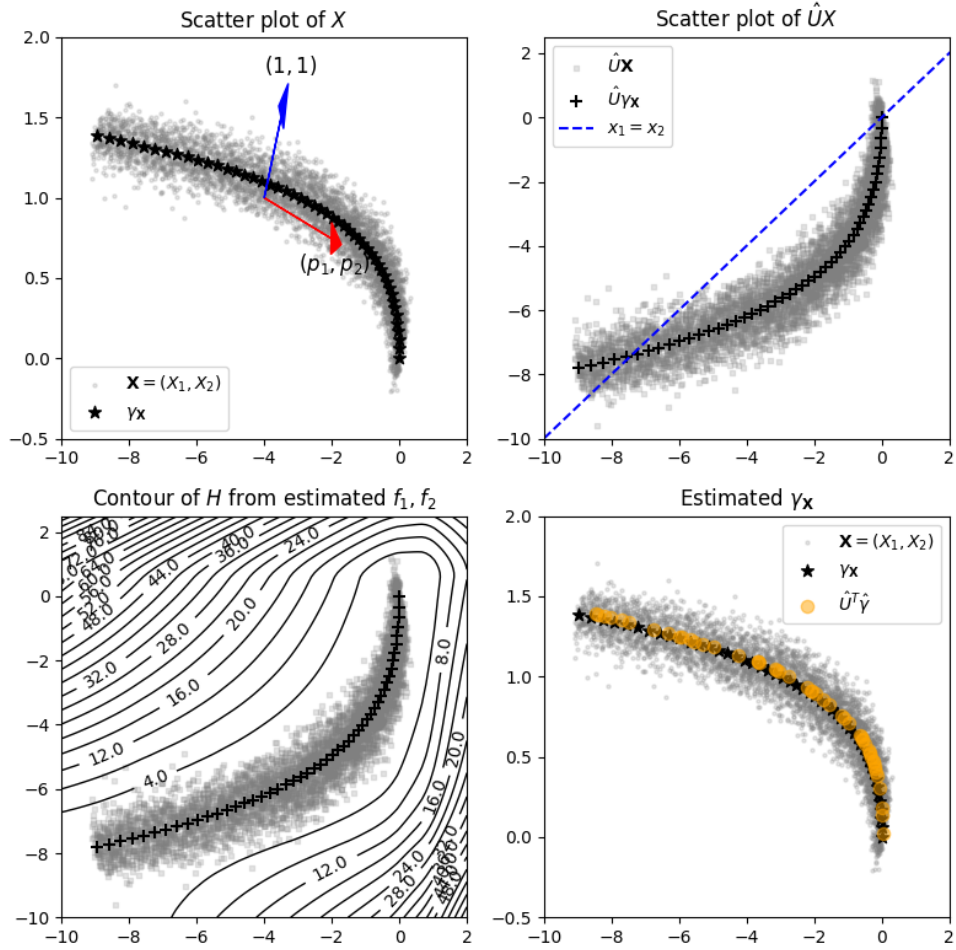


Figure 2: Task 2 for the toy example: (p_1, p_2) is the first principal component, $(1, 1)$ indicates the diagonal direction, and $\gamma_{\mathbf{X}}$ is the true curve associated to \mathbf{X} .

3 Theoretical analysis

In this section, we first show the existence of our curve estimate found from the statistical learning problem and then investigate statistical error bounds for the estimate. The proof and the explicit forms of technical constants appear in Supplementary ???. To highlight the theoretical contributions of our work, we first review key literature in the field. We use the asymptotic notation $a_n = O(b_n)$ (and $a_n = O_p(b_n)$) to imply that a_n/b_n is bounded above by a constant (and with high probability), as n gets larger for the sequences a_n, b_n .

In the first branch of principal curve literature (see Section 1.1), the work of Kégl et al. (2000), assuming the curve has a fixed length on a bounded domain, showed that the rate of convergence is at $O(n^{-1/3})$, but the convergence is in terms of a loss function between data and a curve. That is, the loss function evaluating their empirical minimizer converges to the one of a true curve. More rigorous analysis of the statistical error rate stemmed from the second branch that defines the ridge of the target density as the principal curve. Genovese et al. (2014) provided statistical foundations for Ozertem and Erdogmus (2011). They found a ridge estimator from kernel density estimation converges to the population ridge at $O_p((\log n/n)^{2/(d+8)})$ in the Hausdorff distance, where d is the dimension of data. Moreover, they showed that if data is concentrated on a manifold with Gaussian noise having standard deviation σ in the ambient space, and the ridge estimator aims to extract the manifold, then the rate has an additive error term $O(\sigma^2 \log(1/\sigma))$, relying on the size of the noise, that does not decay by the sample size.

3.1 Existence

To begin with, we show the existence of a solution to the problems (2) and (3) for any distribution of $\mathbf{X} \sim \mu$ where it has the finite second moment.

Theorem 3.1 *Let $\mathcal{D} = \mathcal{C}_{\mathbf{m}}$ in (2) and (3) where $\mathbf{m} = (m_0, m_1, m_2, m_3)$ with $m_i \geq 0$, and*

$$\begin{aligned} \mathcal{C}_{\mathbf{m}} := \{f \in C^2(\mathbb{R}) : |f(0)| \leq m_0, |f'(0)| \leq m_1, 0 \leq f''(x) \leq m_2, \\ |f''(x) - f''(x')| \leq m_3|x - x'| \text{ for all } x, x' \in \mathbb{R}\}. \end{aligned} \quad (6)$$

If $\mathbb{E}_{\mathbf{X} \sim \mu} \|\mathbf{X}\|^2 < \infty$ and $m_2 \geq k - 1$, then solutions to (2) and (3) exist, respectively.

We remark that existing studies of a principal curve particularly for the first branch showed the existence of their principal curves under relatively stronger conditions. The principal

curve with self-consistency condition in Hastie and Stuetzle (1989) guarantees the existence for some specific distributions such as spherically symmetric and ellipsoidal distributions. In Kégl et al. (2000), they showed the existence of a principal curve with a finite second moment, but they further require the curve to have a fixed length on a bounded domain. In contrast, our curve estimation enjoys the existence in more general distributions.

3.2 Statistical error analysis

In this section, we present our primary theoretical results on the statistical error bound of our estimate. We first outline the population model that generates the data. Consider a dimension $k \geq 2$, a maximally monotone curve $\Gamma \subset \mathbb{R}^k$, and a probability distribution $\rho \in \mathcal{P}(\mathbb{R}^k)$ such that $\rho(\Gamma) = 1$. Let $\varepsilon \in \mathcal{P}(\mathbb{R}^k)$ denote the noise distribution with zero mean. Define \mathbf{U} and \mathbf{R} as independent random variables in \mathbb{R}^k , where $\mathbf{U} \sim \rho$ and $\mathbf{R} \sim \varepsilon$, thus $\mathbf{U} \in \Gamma$ and $\mathbb{E}[\mathbf{R}] = \mathbf{0}$. The population model is then described by $\mathbf{X} = \mathbf{U} + \mathbf{R}$ with $\mathbf{X} \sim \mu$, representing the population distribution. Let $\gamma(s) = ((\partial g_i)^{-1}(s))_{i \in [k]}$ parametrize Γ , where $\mathbf{f} = (f_1, \dots, f_k)$ is c -conjugate and exposes Γ , defined as in (??) in Supplementary ??.

Denote $\mathbf{X} = (X_1, \dots, X_k)$ and define $\widehat{\mathbf{X}} := (\mathbf{X}_m)_{m=1}^n = (X_{1,m}, \dots, X_{k,m})$, $m = 1, \dots, n$, as independent and identically distributed (i.i.d.) observations sampled from μ . The empirical data distribution is denoted by $\widehat{\mu} = \sum_{m=1}^n \delta_{\mathbf{X}_m}/n$, where δ_x denotes the Dirac mass at x . Let $\widehat{\mathbf{f}} \in \mathcal{D}^k$ be a c -conjugate solution to (3) with μ replaced by $\widehat{\mu}$, and let $\widehat{\gamma}(s) = ((\partial \widehat{g}_i)^{-1}(s))_{i \in [k]}$ denote the corresponding parametrized monotone curve. Note that although $\widehat{\mu}$ and $\widehat{\gamma}$ depend on the number of samples n , we omit it from the notations for simplicity.

We first establish an upper bound for the *expected empirical MSE*, defined as $E_n^{\text{emp}} = \mathbb{E}[n^{-1} \sum_{m=1}^n \|\gamma(s(\mathbf{X}_m)) - \widehat{\gamma}(s(\mathbf{X}_m))\|^2]$, as stated in the following theorem. This result indicates that our curve estimate becomes more accurate as the noise in the data decreases.

Theorem 3.2 *Let $\mathbf{m} = (m_0, m_1, m_2, m_3) \in \mathbb{R}_{\geq 0}^4$ and $\mathcal{C}_{\mathbf{m}}$ be the class of admissible functions as in (6). Suppose $\Gamma \subset \mathbb{R}^k$ is maximally and strictly monotone, and its associated $\mathbf{f} = (f_i)_{i \in [k]}$, defined in (??), belongs to $(\mathcal{C}_{\mathbf{m}})^k$. Assume $\mathbb{E}\|\mathbf{X}\|^2 < \infty$. Given empirical data $\widehat{\mu}$, let $\widehat{\mathbf{f}}$ minimize (3) with $\mathcal{D} = \mathcal{C}_{\mathbf{m}}$. Then for any data dimension $k \geq 2$ and the number of samples $n \in \mathbb{N}$, we have $E_n^{\text{emp}} \leq C\mathbb{E}[\|\mathbf{R}\|^2]$ where $C > 0$ depends only on m_2, λ , and k . Moreover, if the components of the noise are mutually uncorrelated, i.e., $\mathbb{E}[R_i R_j] = 0$ for every $i \neq j$, then C depends only on m_2 and λ , and not on k .*

We note that this dependence of the empirical error bound on noise size aligns with the argument in Hastie and Stuetzle (1989), which discusses how noise size amplifies the bias of the self-consistent curve, particularly when the curve is an arc of a circle.

We then establish an upper bound for the *generalized MSE*, the estimation error for unseen data $\mathbf{Y} \stackrel{\text{d}}{=} \mathbf{X}$, where \mathbf{Y} is independent of \mathbf{X} , defined as $E_n^{\text{gen}} = \mathbb{E}[\|\gamma(s(\mathbf{Y})) - \widehat{\gamma}(s(\mathbf{Y}))\|^2]$.

Theorem 3.3 *Suppose the assumptions of Theorem 3.2 hold. If μ is compactly supported, then $|E_n^{\text{gen}} - E_n^{\text{emp}}| \leq C'kn^{-1/3}$ where $C' > 0$ depends only on m_1, κ but not on k, n , where κ is the smallest number such that $s(\mathbf{X}) \in [-\kappa, \kappa]$ a.s.. The generalized MSE therefore satisfies*

$$E_n^{\text{gen}} \leq C\mathbb{E}[\|\mathbf{R}\|^2] + C'kn^{-1/3}.$$

Interestingly, our analysis based on the mean squared error conceptually shares similarities with the results of Genovese et al. (2014), particularly for the manifold case. As their rate of convergence, the upper bound of our generalization error is also decomposed by a sample complexity and an additive term proportional to the size of underlying random noises scaled by a technical constant. In our case, the convergence rate is at $O(n^{-1/3})$ in the mean squared error. Also, we remark that our analysis directly tackles the error analysis between true and estimated curves in contrast to Kégl et al. (2000), which advances the curve-level statistical analysis in the first branch of a principal curve literature.

4 Numerical algorithm

In previous sections, we justify the loss function $\mathbb{E}_{\mathbf{X} \sim \mu} [H(U\mathbf{X}; \mathbf{f}) + \lambda \|U\mathbf{X} - \gamma_{\mathbf{f}}(s(U\mathbf{X}))\|^2]$ and its empirical version where \mathbf{f} is in duality to eventually estimate the population monotone curve γ . This section introduces a numerical procedure to obtain the solution of Tasks 1 and 2 to find $\widehat{\gamma}(s) := ((\partial \widehat{g}_i)^{-1}(s))_{i \in [k]}$ where $\widehat{g}_i = \widehat{f}_i + q$ and the diagonal coordinate s . One challenge stems from handling the inf-convolution $(\partial \widehat{g}_i)^{-1} = \nabla(\widehat{f}_i^* \square q)$, since computing the convex conjugate of \widehat{f}_i and performing the required operation together is generally non-trivial. To address this, we incorporate an auxiliary optimization procedure that directly computes the inverse of $\nabla(\widehat{f}_i + q)$. This inverse of gradient is denoted by $\widehat{G}_i^-(s) := (\partial \widehat{g}_i)^{-1}(s)$, representing the target estimate as $\widehat{\gamma}(s) = (\widehat{G}_i^-(s))_{i \in [k]}$. Finally, an additional penalty is placed to enforce the inverse relationship between $\widehat{G}_i^-(s)$ and $\partial \widehat{g}_i$, so the proposed algorithm bypasses to handle the inf-convolution.

To approximate the target functions f_i and G_i^- , we employ neural networks. Neural networks are composite functions constructed from multiple layers of affine transformations and activation functions. Their use in this context offers several advantages. First, neural networks possess a universal approximation property, enabling them to approximate any continuous function arbitrarily well (DeVore et al., 2021). This aligns with the requirements of our framework, where f_i and γ are continuous functions. Also, enforcing the convexity of f_i is straightforward using structural modifications of neural networks.

Denote $\mathbf{G}_-(s) := (G_1^-(s), \dots, G_k^-(s))$ and $\widehat{G}_i := \nabla \widehat{g}_i = \nabla \widehat{f}_i + \text{Id}$. With the consideration of the invertibility constraint for G_i^- , a proposed optimization to implement Task 2 is to solve

$$\min_{\mathbf{f}, \mathbf{G}_-, U} \mathbb{E}_{\widehat{\mu}} [H(U\mathbf{X}; \mathbf{f})] + \lambda \mathbb{E}_{\widehat{\mu}} [\|U\mathbf{X} - \mathbf{G}_-(s)\|^2] + \tau \sum_{i=1}^k \mathbb{E}_{\widehat{\mu}} [|\widehat{G}_i(G_i^-(s)) - s|^2], \quad (7)$$

where $s = \sum_{i=1}^k (U\mathbf{X})_i$, $U \in \mathcal{O}(k)$, $f_i \in \mathcal{NN}_C$, and $G_i^- \in \mathcal{NN}_F$ for all $i = 1, \dots, k$. Recall that the optimization requires two constraints $H(U\mathbf{X}; \mathbf{f}) \geq 0$ and $U^\top U = UU^\top = I$. In the

case of $U = I$, the optimization reduces to solving Task 1. The third term in (7) encodes the monotone structure inherent in $\nabla \widehat{g}_i$, ensuring that the resulting curve, $\widehat{\mathbf{G}}_-$, remains monotone. For \mathcal{NN}_C and \mathcal{NN}_F , we specify 4 hidden layers with 64 nodes and the last layer with 1 output node. The ELU activation function is imposed except for the last layer. The neural networks in \mathcal{NN}_C additionally have the structure of the input convex neural network (Amos et al., 2017) that concatenates the input to all hidden layers and imposes non-negativity constraints on the weight matrices.

Algorithm 1 shows the overall optimization procedures in detail. The superscript (t) denotes the t th iterate of it, \mathbf{X}_i denotes the i th random sample, and $X_{j,i}$ denotes the j th component of \mathbf{X}_i . To handle the nonnegativity constraint for $H(U^{(t)}\mathbf{X}_i; \mathbf{f}^{(t)})$, this work adopts the Lagrangian dual formulation used in Fioretto et al. (2021) that is able to adapt neural networks. This Lagrangian formulation places an inner maximization problem $\lambda_L(0 - H(U^{(t)}\mathbf{X}_i; \mathbf{f}^{(t)}))$ for the variable λ_L . During the iterative computation, λ_L gradually increases according to the violation of the constraint $\max\{-H(U^{(t)}\mathbf{X}_i; \mathbf{f}^{(t)}), 0\}$. We also acknowledge putting a sufficiently large constant λ_L for the constraint. In the algorithm, if $H(U^{(t)}\mathbf{X}_i; \mathbf{f}^{(t)}) \geq 0$ for all i , L^+ is the unbiased estimator of $\mathbb{E}[H(U^{(t)}\mathbf{X}_i; \mathbf{f}^{(t)})]$. For stable updates of the orthogonal transformation matrix, we set $U^{(0)}$ as the inverse of the first PCA component $(p_1, \dots, p_k)^\top$ of \mathbf{X} , so that the first principal component of the transformed data points $(U^{(0)}\mathbf{X}_i)_i$ in the first iteration align with the diagonal, as illustrated in Figure 2. The orthogonality constraint for $U^{(t)}$, i.e., $U^\top U = UU^\top = I$, also adopts the Lagrangian duality with the variable λ_O . Similar to λ_L , λ_O increases such that the resulting transformation approximately satisfies the orthogonality. Algorithm 1 reduces to the implementation of Task 1 by fixing $U^{(t)} = I$ and ignoring the update for orthogonal transformation.

Algorithm 1 adopts the early stopping rule. The n size of random samples is ran-

domly split by training $\widehat{\mu}_{\text{train}} = \{\mathbf{X}_{i_t} : i_t = 1, \dots, n_{\text{train}}\}$ and validation data $\widehat{\mu}_{\text{val}} = \{\mathbf{X}_{i_v} : i_v = 1, \dots, n_{\text{val}}\}$ with $n_{\text{train}} + n_{\text{val}} = n$. Then, in every iteration, models are updated based on $\widehat{\mu}_{\text{train}}$, but the algorithm terminates the training process if the validation error $\mathbb{E}_{\widehat{\mu}_{\text{val}}}[H(U^{(t)}\mathbf{X}; \mathbf{f}^{(t)})] + \lambda \mathbb{E}_{\widehat{\mu}_{\text{val}}}[\|U^{(t)}\mathbf{X} - \mathbf{G}^{(t)}(s)\|^2]$ no longer decreases. Theorem 3.3 justifies this training rule since the theory characterizes that the error gap between training and validation data should be negligible. In this work, the rule does not consider the inverse penalty to align with our theoretical argument. Note that numerous machine learning tasks frequently adopt this rule, as it helps to prevent a model from being overfitted to training data, so models trained on finite samples better represent the underlying population.

5 Simulation

We conduct a comparison study on experimental data sets to verify the performance of our monotone curve-fitting framework. Our study considers Hastie and Stuetzle (1989) and Ozertem and Erdogmus (2011) abbreviated by ‘HS’ and ‘SCMS’ (Subspace Constrained Mean Shift) respectively. These competing methods find general principal curves that are not necessarily monotone, and each approach has different statistical foundations for curve estimation. HS finds a curve that minimizes the mean-squared error on the notion of self-consistency, whereas SCMS finds the ridge of the probability density that is estimated by kernel density estimation.

5.1 Experiment data

The j th experimental data in \mathbb{R}^2 is generated as follows,

$$(X_1^{(j)}(s), X_2^{(j)}(s))^{\top} \sim \mathcal{N}((\mu_1^{(j)}(s), \mu_2^{(j)}(s))^{\top}, (\sigma_1^{(j)}(s), \sigma_{1,2}^{(j)}(s), \sigma_2^{(j)}(s))^{\top}), \quad (8)$$

Algorithm 1 Monotone Curve Estimation with Early Stopping

```

1: Input: Initialized neural networks  $f_1^{(0)}, \dots, f_k^{(0)}, G_1^{-(0)}, \dots, G_k^{-(0)}$ ; Initialize  $U^{(0)} = \text{diag}(1/p_1, \dots, 1/p_k)$ ; Set  $\lambda, \lambda_S \geq 0$ 
   and  $\lambda_L^{(0)} = \lambda_O^{(0)} = 0$ ; the learning rate  $r$  for each component;  $t = 0$ ;  $\text{val}_{\text{prev}} = \text{val}_{\text{current}} = \infty$  (or a sufficiently large number)
2: Output:  $\widehat{\mathbf{G}}_*^* = (G_1^{-(T)}, \dots, G_k^{-(T)})^\top$ ,  $U^* = U^{(T)}$ , and  $\mathbf{f}^* = (f_1^{(T)}, \dots, f_k^{(T)})^\top$ 
3: while  $\text{val}_{\text{prev}} \geq \text{val}_{\text{current}}$  do
4:    $\text{val}_{\text{prev}} \leftarrow \text{val}_{\text{current}}$ 
5:   Set  $s_{i_t} = \sum_{j=1}^k (U^{(t)} \mathbf{X}_{i_t})_j$  for all  $i_t$ 
6:    $L^+ \leftarrow n_{\text{train}}^{-1} \sum_{i_t=1}^{n_{\text{train}}} \max\{H(U^{(t)} \mathbf{X}_{i_t}; \mathbf{f}^{(t)}), 0\}$ 
7:    $L^- \leftarrow n_{\text{train}}^{-1} \sum_{i_t=1}^{n_{\text{train}}} \max\{-H(U^{(t)} \mathbf{X}_{i_t}; \mathbf{f}^{(t)}), 0\}$ 
8:    $R \leftarrow n_{\text{train}}^{-1} \sum_{i_t=1}^{n_{\text{train}}} \|U^{(t)} \mathbf{X}_{i_t} - \mathbf{G}_*^{(t)}(s_{i_t})\|^2$ 
9:    $M \leftarrow n_{\text{train}}^{-1} \sum_{i_t=1}^{n_{\text{train}}} \sum_{j=1}^k |\widehat{G}_j^{(t)}(G_j^{-(t)}(s_{i_t})) - s_{i_t}|^2$ 
10:  for  $j = 1$  to  $k$  do
11:     $f_j^{(t+1)} \leftarrow f_j^{(t)} - r \frac{\partial}{\partial f_j} (L^+ + \tau M + \lambda_L^{(t)} L^-)$ 
12:     $G_j^{-(t+1)} \leftarrow G_j^{-(t)} - r \frac{\partial}{\partial G_j^-} (\lambda R + \tau M)$ 
13:  end for
14:   $\lambda_L^{(t+1)} \leftarrow \lambda_L^{(t)} + r L^-$ 
15:  % Update for Orthogonal Transformation %
16:   $P_O \leftarrow \max\{\sum_{i,j} ((U^{(t),T} U^{(t)} - I)^2 + (U^{(t)} U^{(t),T} - I)^2)_{i,j}, 0\}$ 
17:   $U^{(t+1)} \leftarrow U^{(t)} - r \frac{\partial}{\partial U} (L^+ + \lambda R + \tau M + \lambda_O^{(t)} P_O)$ 
18:   $\lambda_O^{(t+1)} \leftarrow \lambda_O^{(t)} + r P_O$ 
19:  % Compute the validation metric %
20:  Set  $s_{i_v} = \sum_{j=1}^k (U^{(t)} \mathbf{X}_{i_v})_j$  for all  $i_v$ 
21:   $\text{val}_{\text{current}} \leftarrow n_{\text{val}}^{-1} \sum_{i_v=1}^{n_{\text{val}}} \max\{H(U^{(t)} \mathbf{X}_{i_v}; \mathbf{f}^{(t)}), 0\} + \lambda n_{\text{val}}^{-1} \sum_{i_v=1}^{n_{\text{val}}} \|U^{(t)} \mathbf{X}_{i_v} - \mathbf{G}_*^{(t)}(s_{i_v})\|^2$ 
22:   $t \leftarrow t + 1$ 
23: end while
24: Set  $T \leftarrow t$ 

```

where $s \sim S^{(j)}$ is assumed; $(\mu_1^{(j)}(s), \mu_2^{(j)}(s))^\top$ is the j th vector of mean functions w.r.t. s ; $\sigma_1^{(j)}(s)$ and $\sigma_2^{(j)}(s)$ are the variance of each element while $\sigma_{1,2}^{(j)}(s)$ is the covariance between the elements. Note that the mean vector indicates the principal curve. Table 1 summarizes the parameters to generate experimental data sets. To collect data, we first generate $s \sim S^{(j)}$, and $(X_{1,i}^{(j)}(s), X_{2,i}^{(j)}(s))^\top$ is generated based on the evaluated function of μ and σ for $i = 1, \dots, 5000$. Then the data is standardized such that each variable has zero mean and unit standard deviation before fitting the curves. This pre-processing step

improves the performance of HS.

Table 1: Configuration of each experimental data in \mathbb{R}^2

| j | $S^{(j)}$ | $\mu_1^{(j)}$ | $\mu_2^{(j)}$ | $\sigma_1^{(j)}$ | $\sigma_2^{(j)}$ | $\sigma_{1,2}^{(j)}$ |
|-----|------------|------------------|---------------|------------------|------------------|--|
| 1 | Unif(-3,3) | $\exp(s/10) + s$ | $s^3/3 + s$ | 0.1 | 0.1 | $0.1 \times \min\{\cos(s\pi) \exp(s), 1\}$ |
| 2 | Unif(-3,3) | s | s | 0.1 | 0.1 | $0.1 \times \cos(s\pi)$ |
| 3 | Unif(0,3) | $-s^2$ | $\log(s+1)$ | 0.1 | 0.1 | 0.09 |

To also investigate the performance in \mathbb{R}^3 , the above data-generating process (8) is further extended to sample the multivariate normal $(X_1^{(j)}(s), X_2^{(j)}(s), X_3^{(j)}(s))^T$. This three-dimensional random vector inherits the parameters used in Table 1 for $(X_1^{(j)}(s), X_2^{(j)}(s))^T$, and the parameters for $X_3^{(j)}(s)$ and associated dependencies appear in Table 2 where $\sigma_3^{(j)}$ is the standard deviation for $X_3^{(j)}$ and $\sigma_{l,m}^{(j)}$ is the covariance between $X_l^{(j)}$ and $X_m^{(j)}$.

Table 2: Additional parameters for each experimental data in \mathbb{R}^3

| j | $\mu_3^{(j)}$ | $\sigma_3^{(j)}$ | $\sigma_{2,3}^{(j)}$ | $\sigma_{1,3}^{(j)}$ |
|-----|---------------|------------------|----------------------|--|
| 1 | t | 0.1 | 0.05 | $0.1 \times \min\{\sin(t\pi) \exp(t), 1\}$ |
| 2 | t | 0.1 | 0.09 | $0.1 \times \sin(t\pi)$ |
| 3 | t | 0.1 | 0.09 | 0.09 |

5.2 Comparison

To begin with, the implementation of each method is briefly explained. The curves of the competing methods, HS and SCMS, are found through their open source libraries with the default configuration of their algorithms, where SCMS uses the Silverman's rule of thumb for the bandwidth parameter. For ours, the original data $\widehat{\mu}$ with 5000 instances is randomly split by 4500 and 500 to distinguish training $\widehat{\mu}_{\text{train}}$ and validation data $\widehat{\mu}_{\text{val}}$, then Algorithm 1 is implemented. Since HS and SCMS find estimated curves using all data

instances $\widehat{\mu}$, ours also returns the estimated curve by evaluating $U^{*,\top}\widehat{\mathbf{G}}_-(s)$ on the entire data $\widehat{\mu}$. Multiplying $U^{*,\top}$ produces the estimated curve in the original space. The choice of λ and τ is discussed later. To see details of implementation, refer to Supplementary ??.

Visual inspection and quantitative evaluation support the superiority of our approach for finding the ground truth monotone curves. Figure 3 provides a visual comparison of the methods in both \mathbb{R}^2 and \mathbb{R}^3 . HS and ours produce smooth curves; however, SCMS exhibits significant oscillations and erroneously traces data points as curves, particularly around the tails of the distributions. While HS appears to follow the monotone curves reasonably well in cases $j = 1, 2$, but for $j = 3$, it abruptly bends upward near the top left region, significantly deviating from the true curve. Similar phenomena are also observed in the case of \mathbb{R}^3 as well. To evaluate the performance, we calculate averages and standard deviations of the Hausdorff and 2-Wasserstein distance between the estimated and the true curves, abbreviated by Haus. and Wass. respectively, based on 10 independent replicates for each method. All values are rounded up at the 3 decimal point and multiplied by 100 for clarity. Table 3 supports the visual inspections. Ours achieves better evaluation scores compared to the competing methods in general. Note that the Hausdorff distance is particularly useful for assessing the robustness of a method in noisy data. The incorrect curve points of SCMS, which look isolated from the true curve, lead to substantially large Hausdorff distances.

5.2.1 Varying the size of noise

Table 4 summarizes the evaluation scores for the different magnitudes of random noise whose variance and covariance components in (8) are multiplied by σ_f , particularly for the case of $j = 3$. Note that the third experimental data involves more difficult curve estimation than the others intrinsically. In Table 3, all methods show relatively higher errors for $j = 3$.

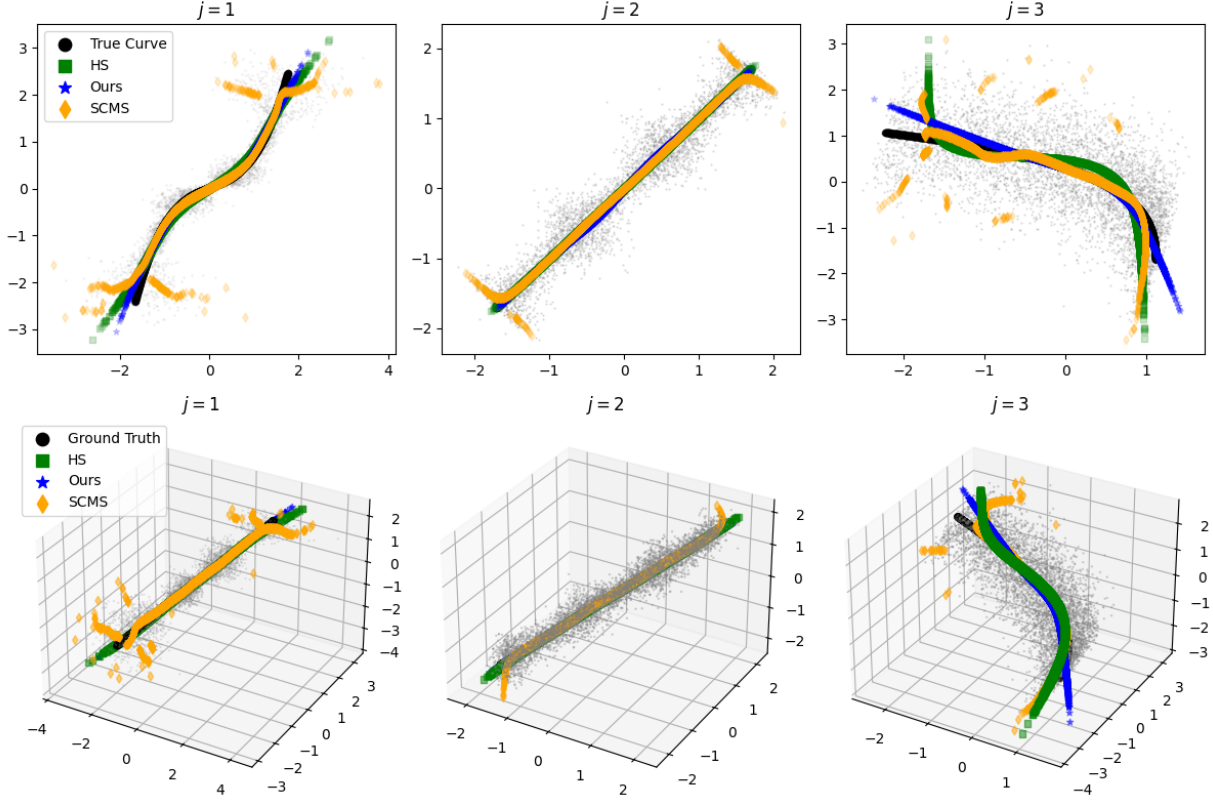


Figure 3: Comparison of three methods on 2 and 3 dimensions: the ground truth curves (black points), Ours (blue stars), SCMS (orange rhombuses), and HS (green rectangles).

Table 3: The number in the parenthesis stands for the standard deviation. Smaller values for each type of score are marked boldly.

| k | j | Ours | | HS | | SCMS | |
|----------------|-----|-------------------------|----------------------|------------------|---------------|------------------|---------------|
| | | Haus.(↓) | Wass.(↓) | Haus.(↓) | Wass.(↓) | Haus.(↓) | Wass.(↓) |
| \mathbb{R}^2 | 1 | 83.141 (10.270) | 0.775 (0.137) | 129.247 (17.985) | 1.420 (0.157) | 205.784 (19.676) | 3.710 (0.305) |
| | 2 | 7.499 (1.686) | 0.196 (0.039) | 15.856 (5.475) | 0.666 (0.129) | 90.283 (14.467) | 1.013 (0.133) |
| | 3 | 137.598 (27.392) | 2.973 (0.397) | 176.840 (25.085) | 8.655 (1.419) | 224.469 (22.693) | 8.582 (0.918) |
| \mathbb{R}^3 | 1 | 74.966 (8.314) | 0.689 (0.141) | 115.325 (17.367) | 1.708 (0.165) | 215.840 (28.041) | 5.181 (0.479) |
| | 2 | 30.062 (3.512) | 0.150 (0.029) | 47.032 (5.645) | 0.461 (0.059) | 91.037 (19.051) | 0.537 (0.051) |
| | 3 | 147.316 (19.486) | 4.588 (0.418) | 197.863 (33.584) | 6.449 (0.493) | 248.761 (19.156) | 7.721 (0.920) |

As shown in Table 4, the three models show improved performance as the noise scale gets smaller. In particular, we observe that ours is still consistently stronger in the Hausdorff

distance but SCMS now becomes stronger in the 2-Wasserstein distance. Tables 3 and 4 highlight that our method tends to achieve more accurate estimation, especially in noisy and complex data exhibiting a roughly monotone shape.

Table 4: For the case of $j = 3$, the variance and covariance components for $j = 3$ are scaled by σ_f . The number in the parenthesis stands for the standard deviation, and the smaller values are marked boldly.

| | | Ours | | HS | | SCMS | |
|----------------|------------|-----------------------|---------------|-----------------|---------------|-----------------|----------------------|
| | σ_f | Haus.(↓) | Wass.(↓) | Haus.(↓) | Wass.(↓) | Haus.(↓) | Wass.(↓) |
| \mathbb{R}^2 | 0.1 | 38.675 (6.315) | 0.919 (0.125) | 60.701 (18.866) | 0.298 (0.025) | 75.654 (12.892) | 0.273 (0.053) |
| | 0.01 | 15.091 (1.947) | 0.380 (0.054) | 17.164 (7.614) | 0.176 (0.016) | 18.963 (6.041) | 0.016 (0.002) |
| \mathbb{R}^3 | 0.1 | 25.138 (4.638) | 0.383 (0.096) | 52.253 (13.588) | 0.417 (0.043) | 75.009 (7.109) | 0.343 (0.035) |
| | 0.01 | 12.350 (2.011) | 0.235 (0.023) | 15.091 (5.152) | 0.289 (0.057) | 15.851 (4.286) | 0.017 (0.002) |

5.3 Model selection

This section discusses how to use the proposed framework in a principled way so that real-world users readily apply our method to their problems.

5.3.1 Choice of λ and τ

Define $L_H = \mathbb{E}_{\widehat{\mu}_{\text{val}}}[H(U^* \mathbf{X}; \mathbf{f}^*)]$ and $L_R = \mathbb{E}_{\widehat{\mu}_{\text{val}}}[\|U^* \mathbf{X} - \widehat{\mathbf{G}}^*(s)\|^2]$. Our proposed strategy is to select λ and τ by minimizing $L_H + L_R$, the sum of the two main validation errors. Alternatively, other criteria can be considered, such as the weighted sum $w_1 L_H + w_2 L_R$ with $w_1 + w_2 = 1$ or the Pareto frontier of (L_H, L_R) , depending on the specific domain knowledge or requirements. While metrics like Hausdorff and Wasserstein distances explicitly measure the estimation quality as the distance between the true and estimated curves, they are often impractical in real-world scenarios since the true curve is typically unknown.

Table 5 summarizes the averages of the evaluation metrics for the 9 combinations of τ and λ in the case of $j = 3$. The table first highlights that our method achieves better Haus. scores compared to the competing methods in all the combinations of τ and λ . Secondly, using λ and τ that achieves the minimum $L_H + L_R$ seems to avoid a relatively poor estimation. For example, as shown in the table, this tuning strategy avoids the choice $(\lambda, \tau) = (1, 10)$ which has a relatively higher $L_H + L_R$. This choice exhibits a significantly worse Wass. score compared to other options in the table, as well as HS and SCMS in Table 3. These findings motivate the adoption of the strategy proposed in this section, with the scores presented in Tables 3 and 4 being derived accordingly. We note that the results of $j = 1$ and $j = 2$ show a similar pattern, and are presented in Supplementary ??.

Table 5: Evaluation metrics for different choices of λ and τ when the data $j = 3$ in \mathbb{R}^2 : In each column of Wass. and Haus., and $L_H + L_R$, bold values indicate the minimum across combinations of λ and τ . Values marked with an asterisk (*) indicate the values of Wass. and Haus. that correspond to the minimum $L_H + L_R$.

| τ | λ | Wass. | Haus. | L_H | L_R | $L_H + L_R$ |
|--------|-----------|-----------------------|------------------------|----------------|----------------|-----------------------|
| 0.1 | 1 | 3.183 (0.420) | 129.313 (22.703) | 30.114 (1.546) | 60.530 (1.617) | 90.645 (2.842) |
| | 10 | 3.084 (0.600) | 134.837 (22.196) | 32.189 (1.764) | 62.591 (1.225) | 94.779 (2.230) |
| | 100 | *2.973 (0.397) | *137.598 (27.392) | 30.138(2.361) | 59.940(2.648) | 90.078 (4.727) |
| 1 | 1 | 3.960 (0.614) | 100.764 (14.479) | 30.870 (2.889) | 62.139 (2.896) | 93.009 (5.675) |
| | 10 | 3.280 (0.468) | 127.209 (21.941) | 30.880 (3.949) | 60.554 (4.251) | 91.434 (8.174) |
| | 100 | 3.310 (0.415) | 137.856 (24.916) | 30.214 (2.876) | 61.174 (3.268) | 91.388 (5.876) |
| 10 | 1 | 8.476 (0.755) | 100.988 (10.723) | 35.569 (2.827) | 68.700 (2.625) | 104.269 (5.265) |
| | 10 | 4.765 (0.512) | 98.660 (16.712) | 31.306 (4.148) | 61.704 (3.705) | 93.010 (7.779) |
| | 100 | 3.275 (0.461) | 132.662 (23.547) | 32.754 (3.470) | 61.122 (3.003) | 93.876 (6.249) |

5.3.2 Estimation with U

Another key consideration is whether to use the orthogonal transformation. Table 6 compares evaluation scores when U is a variable versus when it is fixed as $U = I$. As shown in the table, optimizing the transformation matrix significantly improves estimation accuracy, particularly when the underlying curve is non-increasing. The optimized transformation matrix repositions data points so that each variable exhibits an increasing relationship, allowing the algorithm to identify the increasing curve more effectively in the transformed space. However, if the original data already shows a clear increasing pattern, using the orthogonal transformation is not essential. For instance, in Table 6, only minor improvements are observed for $j = 1$ and $j = 2$ when optimizing U , and even with $U = I$, the results still outperform competing methods in Table 3 in terms of Haus. and Wass. distances.

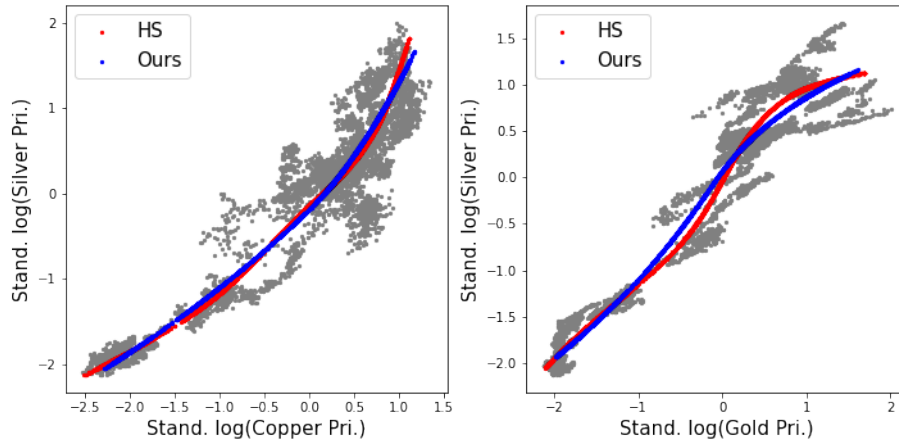
Table 6: Comparison for using the orthogonal transformation in Algorithm 1

| j | Variable U | | Fixed $U = I$ | |
|-----|-------------------------|------------------------|------------------------|------------------------|
| | Haus. (\downarrow) | Wass. (\downarrow) | Haus. (\downarrow) | Wass. (\downarrow) |
| 1 | 83.141 (10.270) | 0.775 (0.137) | 86.543 (14.505) | 0.873 (0.152) |
| 2 | 7.499 (1.686) | 0.196 (0.039) | 8.264 (3.395) | 0.219 (0.074) |
| 3 | 137.598 (27.392) | 2.973 (0.397) | 181.608 (11.925) | 110.020 (4.215) |

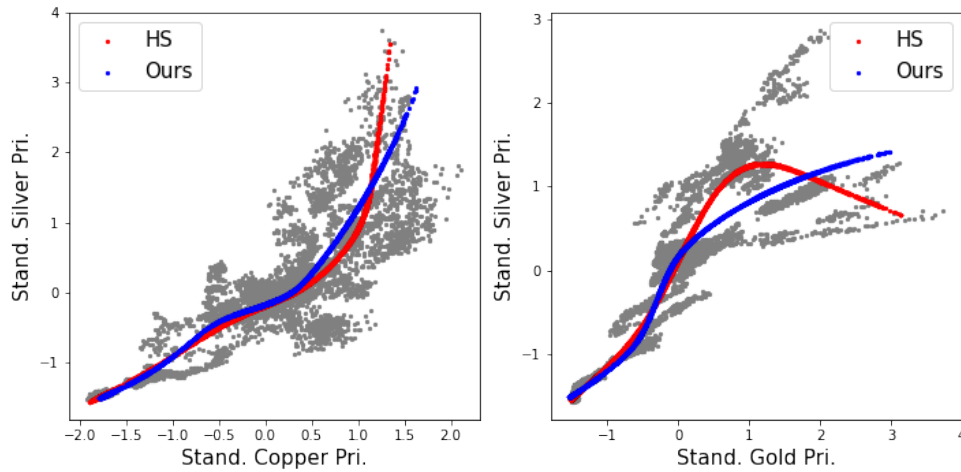
6 Real data application

In this section, we apply the proposed method to two noisy and complex real-world datasets where monotonicity is reasonably assumed or observed by general curve-fitting methods. To evaluate the robustness of our approach, we compare two estimated curves based on different types of variable transformations. Variable transformation, a common preprocessing step in machine learning, is used to stabilize training and meet statistical assumptions. Ideally, a robust curve estimation method should produce consistent results regardless of

the chosen transformation technique, ensuring reliability in the decision-making process.



(a) Prices (Pri.) are standardized (Stand.) after logarithmic transformation ($\log(\cdot)$) before estimating the curves.



(b) Prices (Pri.) are standardized (Stand.) before estimating the curves.

Figure 4: Comparison of commodity prices: the prices of copper, silver and gold. Gray points are observed data points. Ours and HS curves are colored blue and red respectively.

Co-movement of commodity prices Analyzing commodity prices in terms of inter-dependence or reliance on economic indices is an important step toward gaining an in-depth understanding of global economics and financial markets. We apply the proposed method for modeling the future prices of copper, silver, and gold from August 30, 2000, to

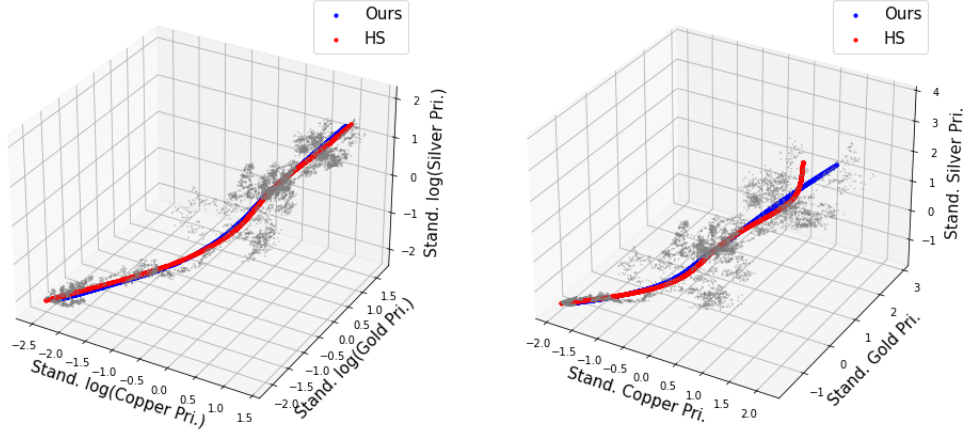


Figure 5: Comparison of commodity prices in \mathbb{R}^3 : (Left) the prices are standardized after logarithmic transformation, and (right) the prices are just standardized before estimation.

November 6, 2024. Each commodity price is retrieved via the Yahoo Finance API in R¹. Rather than seeking economic insights, we attempt to address the advantage of enforcing monotonicity in curve estimation for robust inference by comparing the results to those of HS. To fit monotone curves, we use the same configuration as in the simulation section.

Figures 4 and 5 contrast the two estimated curves in \mathbb{R}^2 and \mathbb{R}^3 respectively. For the case of \mathbb{R}^2 , we compare the price pairs: copper vs silver and gold vs silver. The case of \mathbb{R}^3 finds principal curves penetrating the middle of the three commodity prices. First, since the observed commodity prices tend to become more dispersed as the prices increase, the prices go through the logarithmic transformation and then standardization. Figure 4a displays the estimated HS curves monotonically increasing in both cases. This preceding procedure practically means that an HS curve can play the role of a profile analysis to

¹`quantmod::getSymbols(x, src = "yahoo", from = "2000-08-30", to = "2024-11-06") # Insert x="HG=F" ("SI=F", "GC=F", resp.).`

justify using our monotone curve-fitting framework. Next, we find curves on data points only with standardization to see the impact of transformation on curve estimation. As shown in Figure 4b, while our curve maintains the overall increasing shape, the shape of HS curve is inconsistent compared to Figure 4a. For the comparison between gold and silver prices, the HS curve does not represent the monotonic relationship anymore, which shows that the HS curve is sensitive to transforming variables. For the case of copper and silver in Figure 4b, the downward curvature suddenly increases at 0.5 of **Stand. Copper Pri.**, pushing the curve sharply touches the point at its northernmost tip. This does not look representing the middle of data from our perspective. Figure 5 compares the curves of all the commodities and observes the same phenomenon, addressing that ours enjoys the robustness in terms of variable transformation.

Demand curve of avocado data The Avocado Prices and Sales Volume data² provides a comprehensive overview of avocado market trends in the United States over eight years between 2015 and 2023. The data includes important market information such as average prices, sales volume, and bag sizes for conventional and organic avocados in various regions of the United States. In this work, we are particularly interested in the joint relationship between prices (**AveragePrices**) and sales volume (**TotalVolume**) because these variables can be used to draw a demand curve for the avocado market. In economics, it is commonly believed that product prices and sales volume are inversely related because of the law of demand. We illustrate demand curves for organic avocados in San Francisco and Chicago. The curve of HS is also drawn for comparison.

Figure 6 compares the demand curves of ours and HS. Because sales volume (**TotalVolume**) are on a large scale, we consider transforming it by $\text{TotalVolume}/10000$ and $\log(\text{TotalVolume})$.

²<https://www.kaggle.com/datasets/vakhariapujan/avocado-prices-and-sales-volume-2015-2023>

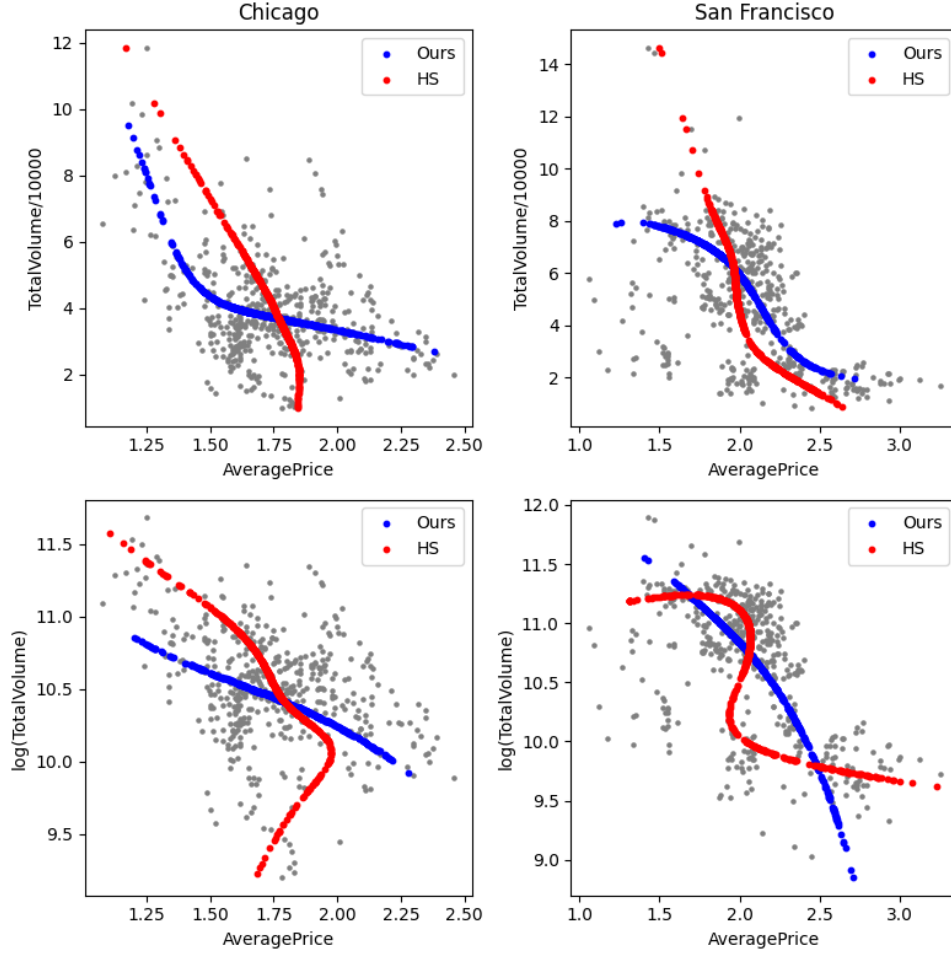


Figure 6: Demand curves: plots in the left are of Chicago and in the right of San Francisco.

HS shows a monotonically decreasing pattern in the case of the linear transformation but nonmonotonic behaviors for the log transformation. In contrast, ours maintains a monotonically decreasing relationship regardless of the type of transformation. Although the curves of San Francisco have slightly different curvatures in higher prices, the overall monotonic shape remains. In general, when developing an operational strategy for a business, accurate and robust estimation of a demand curve is critical because it can be used to optimize pricing strategies and resource allocation in order to maximize potential revenue or profit.

References

- Amos, B., L. Xu, and J. Z. Kolter (2017). Input convex neural networks. In *International conference on machine learning*, pp. 146–155. PMLR.
- Arfaoui, M. and A. Ben Rejeb (2017). Oil, gold, us dollar and stock market interdependencies: a global analytical insight. *European Journal of Management and Business Economics* 26(3), 278–293.
- Banfield, J. D. and A. E. Raftery (1992). Ice floe identification in satellite images using mathematical morphology and clustering about principal curves. *Journal of the American statistical Association* 87(417), 7–16.
- Bartz, S., H. H. Bauschke, H. M. Phan, and X. Wang (2021). Multi-marginal maximal monotonicity and convex analysis. *Mathematical programming* 185, 385–408.
- Bauschke, H. and P. Combettes (2019). Convex analysis and monotone operator theory in hilbert spaces, corrected printing.
- Chen, Y.-C., C. R. Genovese, S. Ho, and L. Wasserman (2015). Optimal ridge detection using coverage risk. *Advances in Neural Information Processing Systems* 28.
- Chen, Y.-C., S. Ho, A. Tenneti, R. Mandelbaum, R. Croft, T. DiMatteo, P. E. Freeman, C. R. Genovese, and L. Wasserman (2015). Investigating galaxy-filament alignments in hydrodynamic simulations using density ridges. *Monthly Notices of the Royal Astronomical Society* 454(3), 3341–3350.
- DeVore, R., B. Hanin, and G. Petrova (2021). Neural network approximation. *Acta Numerica* 30, 327–444.

- Drier, Y., M. Sheffer, and E. Domany (2013). Pathway-based personalized analysis of cancer. *Proceedings of the National Academy of Sciences* 110(16), 6388–6393.
- Duchamp, T. and W. Stuetzle (1996). Extremal properties of principal curves in the plane. *The Annals of Statistics* 24(4), 1511–1520.
- Eberly, D., R. Gardner, B. Morse, S. Pizer, and C. Scharlach (1994). Ridges for image analysis. *Journal of Mathematical Imaging and Vision* 4, 353–373.
- Einbeck, J. and J. Dwyer (2011). Using principal curves to analyse traffic patterns on freeways. *Transportmetrica* 7(3), 229–246.
- Fioretto, F., P. Van Hentenryck, T. W. Mak, C. Tran, F. Baldo, and M. Lombardi (2021). Lagrangian duality for constrained deep learning. In *Machine Learning and Knowledge Discovery in Databases. Applied Data Science and Demo Track: European Conference, ECML PKDD 2020, Ghent, Belgium, September 14–18, 2020, Proceedings, Part V*, pp. 118–135. Springer.
- Genovese, C. R., M. Perone-Pacifico, I. Verdinelli, and L. Wasserman (2014). Nonparametric ridge estimation. *The Annals of Statistics* 42(4), 1511 – 1545.
- Gerber, S. and R. Whitaker (2013). Regularization-free principal curve estimation. *The Journal of Machine Learning Research* 14(1), 1285–1302.
- Ghazanfar, S., C. Guibentif, and J. C. Marioni (2024). Stabilized mosaic single-cell data integration using unshared features. *Nature biotechnology* 42(2), 284–292.
- Hall, P., W. Qian, and D. Titterton (1992). Ridge finding from noisy data. *Journal of Computational and Graphical Statistics* 1(3), 197–211.

- Hastie, T. and W. Stuetzle (1989). Principal curves. *Journal of the American statistical association* 84(406), 502–516.
- Hauberg, S. (2015). Principal curves on riemannian manifolds. *IEEE transactions on pattern analysis and machine intelligence* 38(9), 1915–1921.
- Kang, S. and H.-S. Oh (2024). Probabilistic principal curves on riemannian manifolds. *IEEE Transactions on Pattern Analysis and Machine Intelligence*.
- Kégl, B., A. Krzyzak, T. Linder, and K. Zeger (2000). Learning and design of principal curves. *IEEE transactions on pattern analysis and machine intelligence* 22(3), 281–297.
- Layton, T. B., L. Williams, N. Yang, M. Zhang, C. Lee, M. Feldmann, G. Trujillo, D. Furniss, and J. Nanchahal (2022). A vasculature niche orchestrates stromal cell phenotype through pdgf signaling: Importance in human fibrotic disease. *Proceedings of the National Academy of Sciences* 119(13), e2120336119.
- Lee, J., J.-H. Kim, and H.-S. Oh (2020). Spherical principal curves. *IEEE Transactions on Pattern Analysis and Machine Intelligence* 43(6), 2165–2171.
- Ozertem, U. and D. Erdogmus (2011). Locally defined principal curves and surfaces. *The Journal of Machine Learning Research* 12, 1249–1286.
- Patton, A. J. and A. Timmermann (2010). Monotonicity in asset returns: New tests with applications to the term structure, the capm, and portfolio sorts. *Journal of Financial Economics* 98(3), 605–625.
- Qiao, W. and W. Polonik (2016). Theoretical analysis of nonparametric filament estimation. *The Annals of Statistics* 44(3), 1269 – 1297.

- Qiao, W. and W. Polonik (2021). Algorithms for ridge estimation with convergence guarantees. *arXiv preprint arXiv:2104.12314*.
- Sohn, J., Q. Song, and G. Lin (2024). Fair supervised learning with a simple random sampler of sensitive attributes. In *International Conference on Artificial Intelligence and Statistics*, pp. 1594–1602. PMLR.
- Takei, Y., J. Yun, S. Zheng, N. Ollikainen, N. Pierson, J. White, S. Shah, J. Thomassie, S. Suo, C.-H. L. Eng, et al. (2021). Integrated spatial genomics reveals global architecture of single nuclei. *Nature* 590(7845), 344–350.
- Tibshirani, R. (1992). Principal curves revisited. *Statistics and computing* 2, 183–190.
- Xie, L., K. Lin, S. Wang, F. Wang, and J. Zhou (2018). Differentially private generative adversarial network. *arXiv preprint arXiv:1802.06739*.
- Zhang, Y. and Y.-C. Chen (2023). Linear convergence of the subspace constrained mean shift algorithm: from euclidean to directional data. *Information and Inference: A Journal of the IMA* 12(1), 210–311.